

# Leveraging Foundation Models for Content-Based Medical Image Retrieval in Radiology

Stefan Denner<sup>1,2</sup>, David Zimmerer<sup>1</sup>, Dimitrios Bounias<sup>1,2</sup>, Markus Bujotzek<sup>1,2</sup>, Shuhan Xiao<sup>1,3</sup>, Lisa Kausch<sup>1</sup>, Philipp Schader<sup>1,3</sup>, Tobias Penzkofer<sup>4</sup>, Paul F. Jäger<sup>5,6</sup>, and Klaus Maier-Hein<sup>1,6,7</sup>

<sup>1</sup> Division of Medical Image Computing, German Cancer Research Center (DKFZ), Heidelberg, Germany

<sup>2</sup> Medical Faculty Heidelberg, Heidelberg University, Heidelberg, Germany

<sup>3</sup> Faculty of Mathematics and Computer Science, Heidelberg University, Heidelberg, Germany

<sup>4</sup> Department of Radiology, Charité - Universitätsmedizin Berlin, Berlin, Germany

<sup>5</sup> Interactive Machine Learning Group (IML), German Cancer Research Center (DKFZ), Heidelberg, Germany

<sup>6</sup> Helmholtz Imaging, German Cancer Research Center (DKFZ), Heidelberg, Germany. Pattern Analysis and Learning Group, Department of Radiation Oncology, Heidelberg University Hospital, Heidelberg, Germany

<sup>7</sup> National Center for Tumor Diseases (NCT) Heidelberg, Germany  
`stefan.denner@dkfz-heidelberg.de`

**Abstract.** Content-based image retrieval (CBIR) has the potential to significantly improve diagnostic aid and medical research in radiology. Current CBIR systems face limitations due to their specialization to certain pathologies, limiting their utility. In response, we propose using vision foundation models as powerful and versatile off-the-shelf feature extractors for content-based medical image retrieval. By benchmarking these models on a comprehensive dataset of 1.6 million 2D radiological images spanning four modalities and 161 pathologies, we identify weakly-supervised models as superior, achieving a  $P@1$  of up to 0.594. This performance not only competes with a specialized model but does so without the need for fine-tuning. Our analysis further explores the challenges in retrieving pathological versus anatomical structures, indicating that accurate retrieval of pathological features presents greater difficulty. Despite these challenges, our research underscores the vast potential of foundation models for CBIR in radiology, proposing a shift towards versatile, general-purpose medical image retrieval systems that do not require specific tuning. Our code, dataset splits and embeddings are made publicly available here.

**Keywords:** Medical Image Retrieval · Content-based image retrieval · Foundation Models · Representation learning

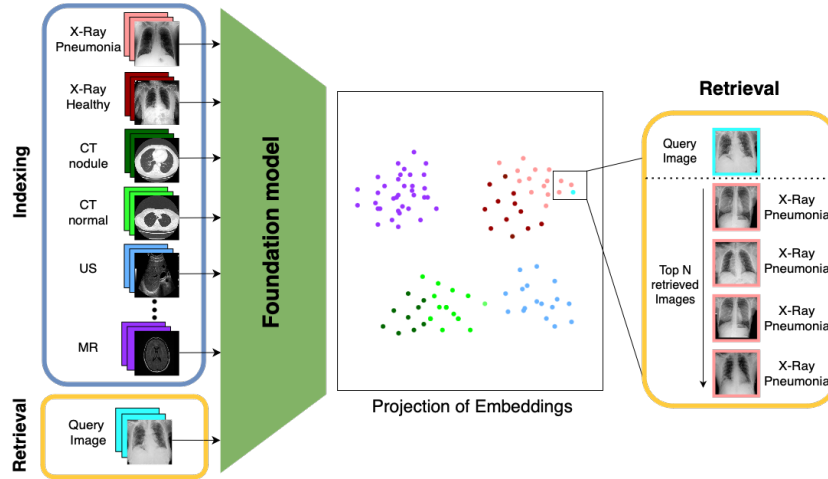


**Fig. 1.** Schema of content-based image retrieval system workflow using foundation models. During indexing, we store the embeddings of the medical images created the foundation model. During retrieval, we compare the embeddings of the query image to those in the index and retrieve the most similar ones.

## 1 Introduction

Content-based image retrieval (CBIR) systems offer significant potential for enhancing teaching, diagnostics and research by the identification of similar case histories and aiding the understanding of pathologies [4,24,26,8]. These systems enable the indexing of large-scale medical-image datasets and the retrieval of images that are visually similar to a query image, thus supporting efficient browsing, searching, and retrieval operations [3]. CBIR systems typically store low-dimensional representations of images in a database and retrieve similar images based on representation similarity [24,16]. In recent years, a key advancement in these systems has been the adoption of deep learning models to encode the visual features of images [9]. However, current CBIR approaches in the medical domain are typically limited to the few pathologies that they were explicitly trained on [4,12,20,18], therefore lacking generalizability to unseen conditions. Furthermore, existing approaches often rely on additional inputs, such as labels [4,12], text [1], or crops [20]. These limitations are in stark contrast to the evolving needs of radiology, which demands a more general and versatile medical image retrieval system capable of handling a broader scope of pathologies without additional input [19,24,8].

However, developing a feature extractor capable of accurately retrieving a wide variety of pathologies presents several challenges. These include the extensive data requirements for training as well as the complexity of preprocessing and the training process itself [31]. A significant obstacle is the nuanced similarity among medical images, where minor yet crucial pathological features may be

overshadowed by the anatomical similarities, leading to potential underrepresentation in the embedding space and failure in pathology differentiation [24,2,9].

To address these challenges, we investigate using vision foundation models as powerful and versatile feature extractors for CBIR. Foundation models, having been exposed to a diverse range of images, are hypothesized to possess a nuanced understanding of relevant features, including those of modality, anatomy, and pathology [32,21,30,1,16]. Using a comprehensive dataset of 1.6 million radiological 2D images across four modalities (CT, MR, X-ray, and US), and 185 classes we answer the following questions:

- What is the performance of vision foundation models as feature extractors for medical image retrieval?
- How does the performance of vision foundation models compare to a specialized, pathology-specific CBIR system?
- What effect does the index size have on the retrieval performance of medical CBIR systems?
- How well do embedding spaces of vision foundation models capture pathological structures?

## 2 Materials and Methods

### 2.1 Datasets

To holistically evaluate foundation models’ performance in medical image retrieval, we combine four public datasets – RadImageNet [23], NIH14 [29], MIMIC [15] and CheXpert [14] – resulting in a comprehensive collection of over 1.6 million 2D images spanning four modalities, 12 anatomical regions, and 185 classes (161 pathological, 24 anatomical). Our dataset has a significant class imbalance with the smallest and largest classes containing 13 and over 226,000 samples, respectively (supplementary Figure 4). We remove duplicates in RadImageNet [23] and harmonize overlapping labels across datasets to ensure consistent labeling. Furthermore, we exclude multi-label samples in all X-Ray datasets to maintain a single-label focus. The dataset preparation also includes a patient-wise split for CheXpert to create a validation set (ratio 90:10 of the training set). For other datasets, we use the provided dataset splits. Details in supplementary Table 5.

### 2.2 Foundation models

We choose a range of foundation models spanning self-supervised, weakly-supervised, and fully-supervised learning schemes, trained on both medical or natural images, ensuring a broad evaluation spectrum (Table 1). Our baselines are ResNet [11] and Vision Transformer (ViT) [7], which are supervised models trained on ImageNet [6]. We use their probability class predictions as feature encodings. We also include the Segment Anything Model (SAM) [17] and its medical adaptation (MedSAM) [21]. Both are supervised prompt-based segmentation models, which showed comparable or even superior performance to fully

**Table 1.** Foundation models utilized for the benchmark.

| Method                   | Architecture | Domain     | #Params. | #Images | Datasets                   |
|--------------------------|--------------|------------|----------|---------|----------------------------|
| <b>Supervised</b>        |              |            |          |         |                            |
| ResNet [11]              | ResNet50     | Natural    | 25 M     | 1.3 M   | IN1K [6]                   |
| ViT [7]                  | ViT-B/16     | Natural    | 91 M     | 14 M    | IN21K [6]                  |
| SAM [17]                 | ViT-B/16     | Natural    | 91 M     | 300 M   | SA-1B [17]                 |
| MedSAM [21]              | ViT-B/16     | Medical    | 91 M     | 1.6 M   | custom [21]                |
| <b>Weakly-Supervised</b> |              |            |          |         |                            |
| CLIP [27]                | ViT-L/14     | Natural    | 300 M    | 400 M   | WIT-400M [27]              |
| MedCLIP [30]             | Swin-T       | Medical    | 29 M     | 600 K   | MIMIC [15] & CheXpert [14] |
| BiomedCLIP [32]          | ViT-B/16     | Biomedical | 91 M     | 15 M    | PMC-15M [32]               |
| <b>Self-Supervised</b>   |              |            |          |         |                            |
| MAE [10]                 | ViT-B/16     | Natural    | 91 M     | 14 M    | IN21K [6]                  |
| DINOv2 [25]              | ViT-B/14     | Natural    | 86 M     | 142 M   | LVD-142M [25]              |

supervised segmentation models [17]. We use the averaged patch tokens of the encoder as embeddings. CLIP [27] is a weakly-supervised learning approach, trained to align the representations of images and texts in a shared embedding space, allowing it to capture a wide range of semantic similarities. MedCLIP [30] and BiomedCLIP [32] are adaptations of CLIP to the medical and biomedical contexts, respectively. For all CLIP-based models, we use the vision encoder representation as embeddings. For the self-supervised model category, we choose ViT-based Masked Autoencoder (MAE) [10] and DINOv2 [25], as they have shown state-of-the-art performance on classification tasks with no or minimal fine-tuning. For both models, we utilize the class token of the ViT as feature encodings.

### 2.3 Leveraging foundation models for image retrieval

Since our goal is to evaluate the effectiveness and versatility of foundation models as feature encoders for medical image retrieval, we utilize them in an off-the-shelf manner, i.e. without any fine-tuning. This approach allows us to rigorously determine the models’ innate capacity to understand and represent medical image pathologies. To this end, we (1) resize the images to the required input size for each model, (2) extract the features as described above, (3) perform  $L2$  normalization on the models’ embeddings, and (4) store these normalized embeddings in a vector database. During retrieval (5), we measure the cosine similarity between the query image encoding and all other image encodings in the index. We retrieve the top  $N$  images with the highest similarity, sorted by descending order.

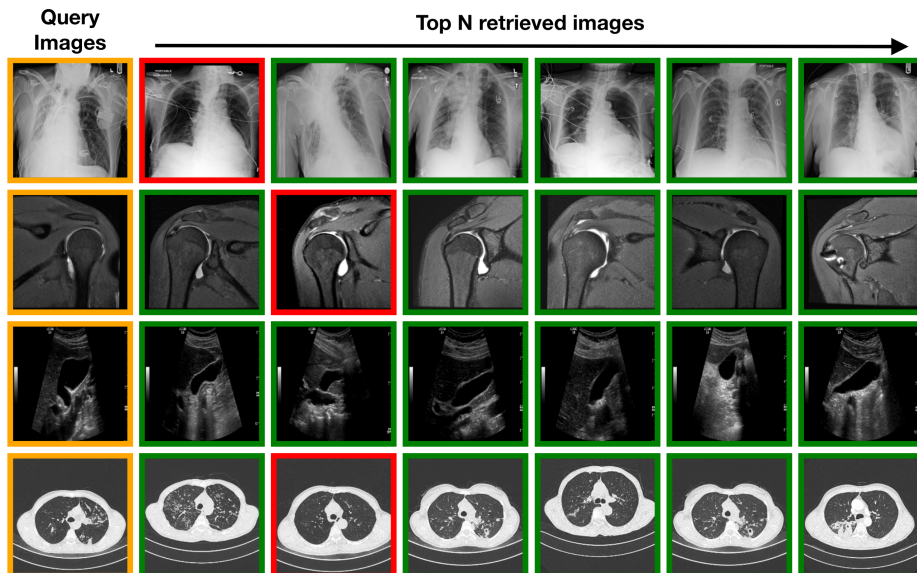


**Fig. 2.** Qualitative results of image retrieval with BiomedCLIP. Rows display the query image highlighted in orange on the left, followed by the six most similar images, sorted by descending similarity. Green frames indicate a match with the query image’s class, red indicates a mismatch.

## 2.4 Evaluation

We measure the retrieval performance between the query image and the top  $N$  retrieved images, quantified by Precision at  $N$  ( $P@N$ ) [22], defined as:

$$P@N = \frac{1}{Q} \sum_{q=1}^Q \frac{1}{N} \sum_{j=1}^N rel_q(j), \quad (1)$$

where  $rel_q(j) \in \{0, 1\}$  is the relevance of the  $j$ -th image for the  $q$ -th query,  $Q$  is the number of queries and  $N \in \{1, 3, 5, 10\}$ . In our setting, an image is considered relevant if it belongs to the same class as the query image. To gain a more comprehensive understanding of our model’s performance, especially for classes with fewer examples, we calculate both micro- and macro-averaged scores. Micro-averaging treats all samples equally, regardless of their class. It measures the average score across all samples. Macro-averaging focuses on each class individually. It first calculates the average score per class, and then averages those class scores. This approach is crucial for imbalanced datasets because it prevents the dominant class from skewing the overall performance and provides a fair evaluation of how well the model performs on less frequent classes.

**Table 2.** Retrieval performance of the evaluated models on the combined dataset.

|                   | Sample-wise (micro) |              |              |              | Class-wise (macro) |              |              |              |
|-------------------|---------------------|--------------|--------------|--------------|--------------------|--------------|--------------|--------------|
|                   | <b>P@1</b>          | <b>P@3</b>   | <b>P@5</b>   | <b>P@10</b>  | <b>P@1</b>         | <b>P@3</b>   | <b>P@5</b>   | <b>P@10</b>  |
| <b>ResNet</b>     | 0.544               | 0.538        | 0.535        | 0.529        | 0.204              | 0.193        | 0.189        | 0.182        |
| <b>ViT</b>        | 0.560               | 0.554        | 0.550        | 0.543        | 0.217              | 0.204        | 0.199        | 0.190        |
| <b>SAM</b>        | 0.520               | 0.517        | 0.515        | 0.511        | 0.197              | 0.187        | 0.182        | 0.175        |
| <b>MedSAM</b>     | 0.489               | 0.483        | 0.478        | 0.470        | 0.154              | 0.146        | 0.142        | 0.134        |
| <b>CLIP</b>       | <u>0.571</u>        | <u>0.567</u> | <u>0.565</u> | <u>0.559</u> | 0.222              | <u>0.213</u> | <u>0.209</u> | <u>0.202</u> |
| <b>MedCLIP</b>    | 0.566               | 0.561        | 0.559        | 0.554        | <u>0.223</u>       | 0.211        | 0.205        | 0.198        |
| <b>BiomedCLIP</b> | <b>0.594</b>        | <b>0.590</b> | <b>0.588</b> | <b>0.583</b> | <b>0.240</b>       | <b>0.230</b> | <b>0.224</b> | <b>0.217</b> |
| <b>MAE</b>        | 0.513               | 0.507        | 0.503        | 0.497        | 0.183              | 0.177        | 0.172        | 0.166        |
| <b>DINOv2</b>     | 0.553               | 0.548        | 0.545        | 0.540        | 0.219              | 0.204        | 0.199        | 0.192        |
| <b>X-MIR</b>      | 0.478               | 0.471        | 0.466        | 0.457        | 0.149              | 0.142        | 0.138        | 0.131        |

**Table 3.** Retrieval performance on the COVID-19 chest X-ray dataset.

|                   | Micro        |              |              |              | Macro        |              |              |              |
|-------------------|--------------|--------------|--------------|--------------|--------------|--------------|--------------|--------------|
|                   | <b>P@1</b>   | <b>P@3</b>   | <b>P@5</b>   | <b>P@10</b>  | <b>P@1</b>   | <b>P@3</b>   | <b>P@5</b>   | <b>P@10</b>  |
| <b>DenseNet</b>   | 0.811        | 0.828        | 0.831        | 0.820        | 0.811        | 0.828        | 0.830        | 0.820        |
| <b>BiomedCLIP</b> | <u>0.913</u> | <u>0.923</u> | <u>0.910</u> | <u>0.921</u> | <u>0.914</u> | <u>0.924</u> | <u>0.910</u> | <u>0.921</u> |
| <b>X-MIR</b>      | <b>0.954</b> | <b>0.934</b> | <b>0.934</b> | <b>0.932</b> | <b>0.954</b> | <b>0.933</b> | <b>0.934</b> | <b>0.931</b> |

### 3 Results and Discussion

**Retrieval performance of foundation models.** Evaluating the retrieval performance of the foundation models on the combined dataset, we observe that BiomedCLIP achieves the highest score across all metrics (Table 2; qualitative results in Figure 2; t-SNE visualization in supplementary Figure 5). In general, weakly-supervised approaches outperform other training schemes. Segmentation models (SAM and MedSAM) show lower performance, suggesting their embeddings are not well-suited for medical image retrieval. Furthermore, medical adaptations (MedSAM and MedCLIP) fail to surpass their natural image counterparts (SAM and CLIP), indicating that their embeddings don’t generalize. The superior performance of CLIP-based approaches can probably be attributed to its training objective of semantically meaningful aligning the representations of images and texts. BiomedCLIP in particular performs well, probably due to its exposure to a wide variety of biomedical image-text pairs, leading to a nuanced understanding of pathologies, which is reflected in the embedding space. However, sample-wise scores are significantly higher than class-wise scores across all models, 0.594 and 0.240 for BiomedCLIP  $P@1$ , respectively.

**Comparison to a specialized medical image retrieval system.** To contextualize the efficacy of employing vision foundation models as feature extractors, it is critical to benchmark their performance against image retrieval systems designed for a narrower spectrum of pathologies. We identified only one publicly

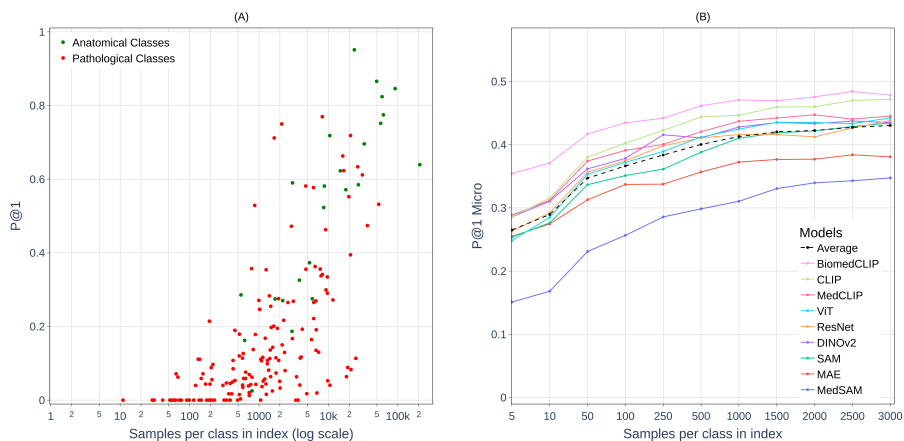


**Fig. 3.** Effect of the number of samples per class in the index on the retrieval performance. (A) Class-wise performance ( $P@1$ ) of BiomedCLIP. Color encoded are anatomical (green) and pathological (red) classes. (B) Sample-wise performance ( $P@1$  micro) of the foundation models with varying numbers of samples per class in the index.

available radiological image retrieval system that operates without requiring additional user input: X-MIR by Hu et al. [12], which utilizes a DenseNet121 [13] trained on a COVID-19 chest X-ray dataset [28] for the retrieval of pneumonia, Covid-19, and normal cases.

Our evaluation unfolds in two phases. Firstly, we evaluate X-MIR on our combined dataset to highlight its limited generalizability to unseen classes (Table 2). Secondly, we evaluate the best performing foundation model on our combined dataset, BiomedCLIP, on the COVID-19 chest X-ray dataset [28], which X-MIR was specifically trained on.<sup>1</sup> Despite BiomedCLIP not being fine-tuned on this dataset, it closely rivals X-MIR’s specialized performance, underscoring the versatility and robustness of foundation models in broader medical image retrieval applications.

**Effect of index size on retrieval performance.** As noted in Section 3, there is a discrepancy between class-wise and sample-wise scores indicating higher performance for more frequent classes on our combined dataset. In Figure 3 A we show, exemplary for BiomedCLIP, that classes with more samples in the index yield higher  $P@1$ . Additionally, our findings show superior performance for anatomical over pathological classes, highlighting the model’s challenges in accurately retrieving pathological structures.

<sup>1</sup> Given updates to the dataset since its initial publication, we evaluate the X-MIR model on a subset of the original dataset, noting discrepancies from the originally reported results.

**Table 4.** Performance of the foundation models on the combined dataset using kNN and linear classification.

|                   | kNN          |              |              |              | Linear       |              |              |              |
|-------------------|--------------|--------------|--------------|--------------|--------------|--------------|--------------|--------------|
|                   | Micro        |              | Macro        |              | Micro        |              | Macro        |              |
|                   | AURPC        | F1           | AURPC        | F1           | AURPC        | F1           | AURPC        | F1           |
| <b>ResNet</b>     | 0.630        | 0.623        | 0.211        | 0.203        | 0.706        | 0.648        | 0.278        | 0.262        |
| <b>ViT</b>        | 0.644        | 0.633        | 0.220        | 0.210        | <u>0.734</u> | <u>0.668</u> | <u>0.300</u> | <u>0.275</u> |
| <b>SAM</b>        | 0.588        | 0.599        | 0.200        | 0.186        | 0.571        | 0.556        | 0.163        | 0.113        |
| <b>MedSAM</b>     | 0.561        | 0.567        | 0.151        | 0.139        | 0.497        | 0.492        | 0.100        | 0.060        |
| <b>CLIP</b>       | <u>0.673</u> | <u>0.648</u> | <u>0.243</u> | <u>0.221</u> | <b>0.743</b> | <b>0.674</b> | <b>0.308</b> | <b>0.278</b> |
| <b>MedCLIP</b>    | 0.668        | 0.643        | 0.241        | 0.212        | 0.720        | 0.660        | 0.286        | 0.246        |
| <b>BiomedCLIP</b> | <b>0.711</b> | <b>0.667</b> | <b>0.269</b> | <b>0.231</b> | 0.713        | 0.651        | 0.273        | 0.232        |
| <b>MAE</b>        | 0.627        | 0.602        | 0.203        | 0.172        | 0.692        | 0.636        | 0.251        | 0.215        |
| <b>DINOv2</b>     | 0.654        | 0.630        | 0.229        | 0.201        | 0.722        | 0.659        | 0.285        | 0.268        |

To investigate whether retrieval performance reaches saturation with a specific number of samples per class in the index, we conduct an ablation study focusing on classes with over 3000 samples, comprising 64 classes (42 pathological and 22 anatomical). We standardize the query dataset size to the smallest class, containing 38 samples per class. Then, we randomly select  $N$  cases per class, where  $N$  ranges from 5 to 3000, to populate the index and conduct retrievals using the fixed query set.

For the best models, P@1 starts saturating at around 1000 samples per class in the index (Figure 3 B). This finding suggests, that up to 1000 samples per class, providing more samples improves the retrieval performance. However, beyond 1000 samples, additional samples do not significantly improve retrieval outcomes, pointing to a need for advancements in the models’ clustering capabilities for performance gains.

**Analysis of the embedding space** While image retrieval directly aims to find similar images, it inherently relies on the quality of the underlying embedding space. By analyzing the embedding space through classification tasks, we gain a deeper understanding of the models’ ability to capture relevant features for the retrieval task [22].

We employ k-nearest neighbors (kNN) classification [5] to evaluate clustering within the embedding space, determining the clustering efficacy of similar images [22]. Additionally, a single-layer linear classifier trained on these representations helps assess whether the embedding space holds classification-relevant features, serving as a benchmark for feature quality. Classification performance is measured by F1-Score and AUPRC to adjust for dataset class imbalance.

Overall, coherent with section 3, BiomedCLIP achieves the best kNN classification performance, suggesting the best clustering of pathological structures in the embedding space (Table 3). However, CLIP surpasses all models in linear classification, indicating that even without finetuning it encodes relevant features for pathological structures more effectively, potentially leading to superior

retrieval performance. Conversely, some (self-)supervised models like DINOv2 and ViT exhibit strong performance in linear classification despite not performing exceptionally well in the retrieval task itself, demonstrating their potential capability as feature extractors for image retrieval after fine-tuning with medical imaging data.

## 4 Conclusion

In this work, we have demonstrated the effectiveness of utilizing vision foundation models as powerful and versatile feature extractors for content-based medical image retrieval, benchmarking their performance across an extensive dataset of over 1.6 million radiological 2D images, spanning four modalities and 185 classes. Our analysis highlights the promising off-the-shelf capabilities of weakly-supervised models, especially BiomedCLIP, in providing superior feature extraction performance, rivaling that of specialized models. Through comprehensive ablation studies, we have gained valuable insights into the clustering and feature extraction capabilities of these models. The encouraging outcomes of our research strongly support the pursuit of further exploration into even more advanced vision foundation models, that can accurately understand and represent pathological similarities. We hope that our publicly shared resources – code, datasets, and embeddings – facilitate future benchmarking of foundation models for medical image retrieval.

## Acknowledgments

Funded by "NUM 2.0" (FKZ: 01KX2121)

## References

1. Abacha, A.B., Santamaria-Pang, A., Lee, H.H., Merkow, J., Cai, Q., Devarakonda, S.T., Islam, A., Gong, J., Lungren, M.P., Lin, T., et al.: 3d-mir: A benchmark and empirical study on 3d medical image retrieval in radiology. arXiv preprint arXiv:2311.13752 (2023)
2. Chen, C., Lu, M.Y., Williamson, D.F., Chen, T.Y., Schaumberg, A.J., Mahmood, F.: Fast and scalable search of whole-slide images via self-supervised deep learning. *Nature Biomedical Engineering* **6**(12), 1420–1434 (2022)
3. Chen, W., Liu, Y., Wang, W., Bakker, E.M., Georgiou, T., Fieguth, P., Liu, L., Lew, M.S.: Deep learning for instance retrieval: A survey. *IEEE Transactions on Pattern Analysis and Machine Intelligence* (2022)
4. Choe, J., Hwang, H.J., Seo, J.B., Lee, S.M., Yun, J., Kim, M.J., Jeong, J., Lee, Y., Jin, K., Park, R., et al.: Content-based image retrieval by using deep learning for interstitial lung disease diagnosis with chest ct. *Radiology* **302**(1), 187–197 (2022)
5. Cover, T., Hart, P.: Nearest neighbor pattern classification. *IEEE transactions on information theory* **13**(1), 21–27 (1967)

6. Deng, J., Dong, W., Socher, R., Li, L.J., Li, K., Fei-Fei, L.: Imagenet: A large-scale hierarchical image database. In: 2009 IEEE conference on computer vision and pattern recognition. pp. 248–255. Ieee (2009)
7. Dosovitskiy, A., Beyer, L., Kolesnikov, A., Weissenborn, D., Zhai, X., Unterthiner, T., Dehghani, M., Minderer, M., Heigold, G., Gelly, S., et al.: An image is worth 16x16 words: Transformers for image recognition at scale. arXiv preprint arXiv:2010.11929 (2020)
8. Dubey, S.R.: A decade survey of content based image retrieval using deep learning. *IEEE Transactions on Circuits and Systems for Video Technology* **32**(5), 2687–2704 (2021)
9. Gordo, A., Almazán, J., Revaud, J., Larlus, D.: Deep image retrieval: Learning global representations for image search. In: *Computer Vision–ECCV 2016: 14th European Conference, Amsterdam, The Netherlands, October 11–14, 2016, Proceedings, Part VI 14*. pp. 241–257. Springer (2016)
10. He, K., Chen, X., Xie, S., Li, Y., Dollár, P., Girshick, R.: Masked autoencoders are scalable vision learners. In: *Proceedings of the IEEE/CVF conference on computer vision and pattern recognition*. pp. 16000–16009 (2022)
11. He, K., Zhang, X., Ren, S., Sun, J.: Deep residual learning for image recognition. In: *Proceedings of the IEEE conference on computer vision and pattern recognition*. pp. 770–778 (2016)
12. Hu, B., Vasu, B., Hoogs, A.: X-mir: Explainable medical image retrieval. In: *Proceedings of the IEEE/CVF Winter Conference on Applications of Computer Vision*. pp. 440–450 (2022)
13. Huang, G., Liu, Z., Van Der Maaten, L., Weinberger, K.Q.: Densely connected convolutional networks. In: *Proceedings of the IEEE conference on computer vision and pattern recognition*. pp. 4700–4708 (2017)
14. Irvin, J., Rajpurkar, P., Ko, M., Yu, Y., Ciurea-Ilcus, S., Chute, C., Marklund, H., Haghgoo, B., Ball, R., Shpanskaya, K., et al.: Chexpert: A large chest radiograph dataset with uncertainty labels and expert comparison. In: *Proceedings of the AAAI conference on artificial intelligence*. vol. 33, pp. 590–597 (2019)
15. Johnson, A.E., Pollard, T.J., Shen, L., Lehman, L.w.H., Feng, M., Ghassemi, M., Moody, B., Szolovits, P., Anthony Celi, L., Mark, R.G.: MIMIC-III, a freely accessible critical care database. *Scientific data* **3**(1), 1–9 (2016)
16. Jush, F.K., Truong, T., Vogler, S., Lenga, M.: Medical image retrieval using pre-trained embeddings. arXiv preprint arXiv:2311.13547 (2023)
17. Kirillov, A., Mintun, E., Ravi, N., Mao, H., Rolland, C., Gustafson, L., Xiao, T., Whitehead, S., Berg, A.C., Lo, W.Y., et al.: Segment anything. arXiv preprint arXiv:2304.02643 (2023)
18. Kobayashi, K., Gu, L., Hataya, R., Mizuno, T., Miyake, M., Watanabe, H., Takahashi, M., Takamizawa, Y., Yoshida, Y., Nakamura, S., et al.: Sketch-based semantic retrieval of medical images. *Medical Image Analysis* **92**, 103060 (2024)
19. Langlotz, C.P.: The future of ai and informatics in radiology: 10 predictions (2023)
20. Lee, H.H., Santamaria-Pang, A., Merkow, J., Oktay, O., Pérez-García, F., Alvarez-Valle, J., Tarapov, I.: Region-based contrastive pretraining for medical image retrieval with anatomic query. arXiv preprint arXiv:2305.05598 (2023)
21. Ma, J., He, Y., Li, F., Han, L., You, C., Wang, B.: Segment anything in medical images. *Nature Communications* **15**(1), 654 (2024)
22. Manning, C.D.: An introduction to information retrieval. Cambridge university press (2009)

23. Mei, X., Liu, Z., Robson, P.M., Marinelli, B., Huang, M., Doshi, A., Jacobi, A., Cao, C., Link, K.E., Yang, T., et al.: Radimagenet: an open radiologic deep learning research dataset for effective transfer learning. *Radiology: Artificial Intelligence* **4**(5), e210315 (2022)
24. Müller, H., Michoux, N., Bandon, D., Geissbuhler, A.: A review of content-based image retrieval systems in medical applications—clinical benefits and future directions. *International journal of medical informatics* **73**(1), 1–23 (2004)
25. Oquab, M., Darcet, T., Moutakanni, T., Vo, H., Szafraniec, M., Khalidov, V., Fernandez, P., Haziza, D., Massa, F., El-Nouby, A., et al.: Dinov2: Learning robust visual features without supervision. *arXiv preprint arXiv:2304.07193* (2023)
26. Qayyum, A., Anwar, S.M., Awais, M., Majid, M.: Medical image retrieval using deep convolutional neural network. *Neurocomputing* **266**, 8–20 (2017)
27. Radford, A., Kim, J.W., Hallacy, C., Ramesh, A., Goh, G., Agarwal, S., Sastry, G., Askell, A., Mishkin, P., Clark, J., et al.: Learning transferable visual models from natural language supervision. In: *International conference on machine learning*. pp. 8748–8763. PMLR (2021)
28. Wang, L., Lin, Z.Q., Wong, A.: Covid-net: A tailored deep convolutional neural network design for detection of covid-19 cases from chest x-ray images. *Scientific reports* **10**(1), 19549 (2020)
29. Wang, X., Peng, Y., Lu, L., Lu, Z., Bagheri, M., Summers, R.M.: Chestx-ray8: Hospital-scale chest x-ray database and benchmarks on weakly-supervised classification and localization of common thorax diseases. In: *Proceedings of the IEEE conference on computer vision and pattern recognition*. pp. 2097–2106 (2017)
30. Wang, Z., Wu, Z., Agarwal, D., Sun, J.: Medclip: Contrastive learning from unpaired medical images and text. *arXiv preprint arXiv:2210.10163* (2022)
31. Willemink, M.J., Koszek, W.A., Hardell, C., Wu, J., Fleischmann, D., Harvey, H., Folio, L.R., Summers, R.M., Rubin, D.L., Lungren, M.P.: Preparing medical imaging data for machine learning. *Radiology* **295**(1), 4–15 (2020)
32. Zhang, S., Xu, Y., Usuyama, N., Bagga, J., Tinn, R., Preston, S., Rao, R., Wei, M., Valluri, N., Wong, C., et al.: Large-scale domain-specific pretraining for biomedical vision-language processing. *arXiv preprint arXiv:2303.00915* (2023)

**Table 5.** Datasets utilized for the benchmark. For image retrieval, train dataset was used for indexing and test dataset for querying/retrieval. For kNN classification, validation dataset was for determining the best  $K$ . For linear classification, validation dataset was used for early stopping.

| Dataset          | Modality | Train     | Val     | Test    | Pathology/<br>Anatomy classes |
|------------------|----------|-----------|---------|---------|-------------------------------|
| NIH14 [29]       | XR       | 66,192    | 7,279   | 17,853  | 14/1                          |
| MIMIC [15]       | XR       | 229,597   | 1,775   | 2,473   | 12/1                          |
| CheXpert [14]    | XR       | 50,194    | 5,587   | 54      | 12/1                          |
| RadImageNet [23] | MR       | 460,479   | 48,820  | 57,103  | 109/7                         |
|                  | CT       | 202,521   | 24,660  | 63,198  | 32/2                          |
|                  | US       | 313,569   | 27,417  | 31,072  | 14/1                          |
| Total            |          | 1,322,552 | 115,538 | 171,753 | 161/24                        |

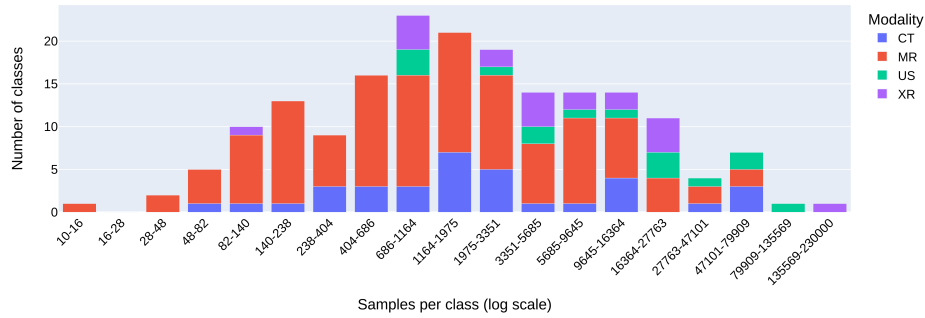


**Fig. 4.** Class imbalance of the combined dataset.

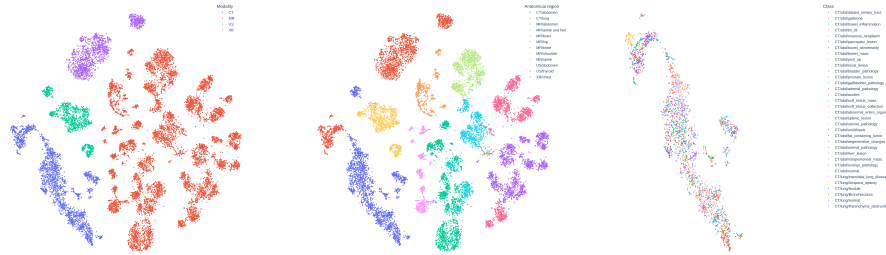


**Fig. 5.** t-SNE projections of the BiomedCLIP embeddings of the combined dataset. Left: Color encoded are modalities. Center: Color encoded are anatomical structures. Right: Filtered for CT images only. Color encoded are pathologies.

**Table 6.** Training details for the linear classifier.

|                |          |
|----------------|----------|
| Epochs         | 100      |
| Early stopping | 20       |
| Learning rate  | 1.00E-03 |
| Optimizer      | AdamW    |

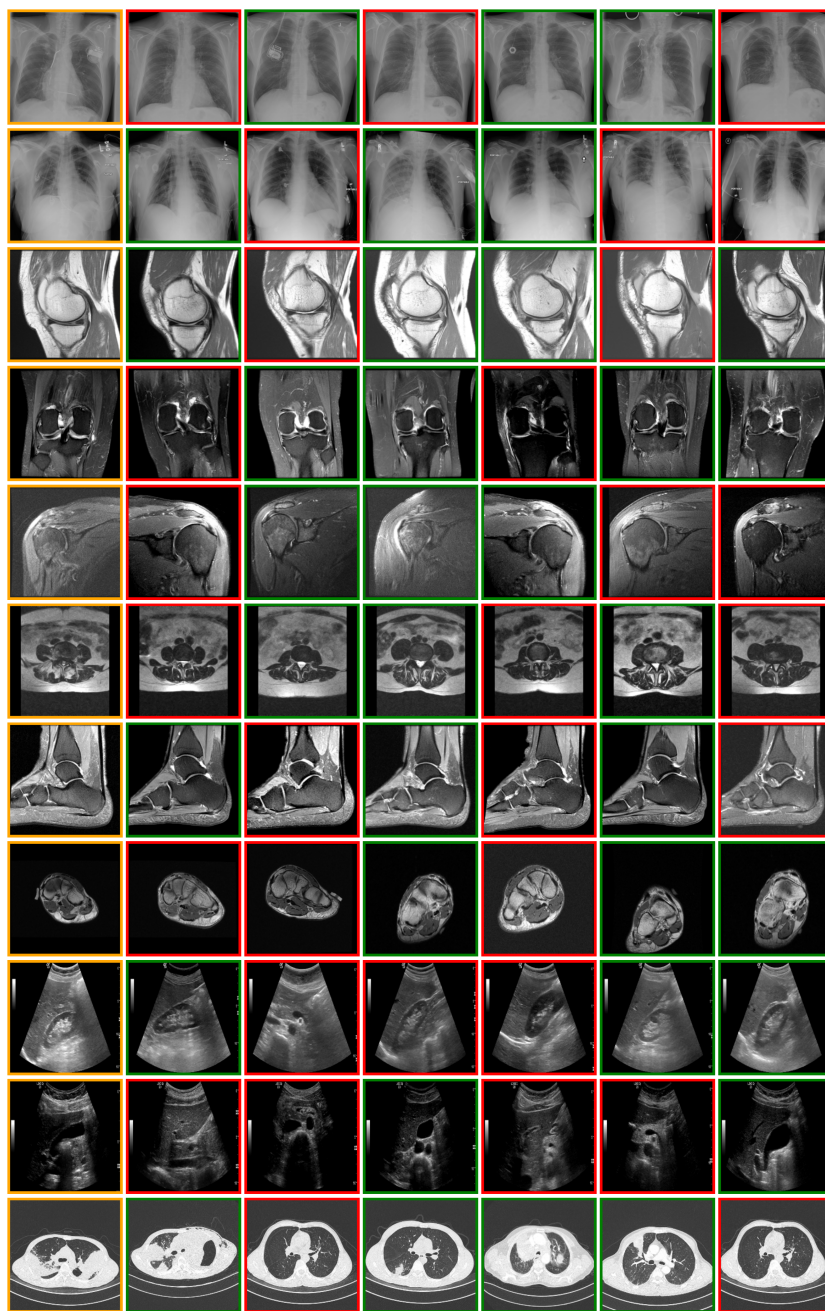


**Fig. 6.** Qualitative results of image retrieval with BiomedCLIP. Rows display the query image highlighted in orange on the left, followed by the six most similar images, sorted by descending similarity. Green frames indicate a match with the query image's class, red indicates a mismatch.